International Journal of Applied Electromagnetics and Mechanics 12 (2000) 151–164
IOS Press

Automated analysis of rotating probe multi-frequency eddy current data from steam generator tubes

P. Xiang[b], S. Ramakrishnan[b], X. Cai[b], P. Ramuhalli[b], R. Polikar[b], S.S. Udpa[a] and L. Udpa[b]
[a]*Department of Electrical and Computer Engineering, Michigan State University, East Lansing, MI 48824-1226, USA*
[b]*Materials Assessment Research Group, Department of Electrical and Computer Engineering, Iowa State University, Ames, IA 50011, USA*

Abstract. An algorithm is presented for the automated analysis of rotating probe multifrequency eddy current data obtained from nuclear power plant steam generator tubes (SGT). The algorithm consists of four steps, namely, a preprocessing stage for conditioning the data, a decision tree based feature extraction stage for identifying relevant features for analysis, a neural network based classification stage for identifying signals from various defect types and benign structures, and finally a blind deconvolution based characterization stage for accurately estimating the size and orientation of the detected defects. This algorithm is optimized to maximize the probability of detection (POD), while keeping the number of false alarms (PFA) at a minimum. Initial results presented in this paper look very promising and demonstrate the effectiveness of the proposed algorithm.

1. Introduction

Heat exchanger tubes in nuclear power plant steam generators are continuously exposed to a very harsh environment. The degradation caused by these environmental effects range from mechanical wear between tubes and tube support plates, outer diameter stress corrosion cracking (ODSCC), pitting, denting and primary water stress corrosion cracking (PWSCC) to inter granular attack (IGA) resulting in tube thinning and multiple crack-like flaws. Eddy current testing (ECT) of steam generator tubing (SGT) is performed extensively in order to detect and size flaws [1]. A typical SGT geometry is shown in Fig. 1. Eddy current probes commonly used for SGT testing include bobbin coil probes and in recent years, rotating coil probes. Multifrequency rotating coil probes have several advantages:

- unwanted signals from structures such as tube support plates can be cancelled using a mixing algorithm,
- flaws can be located more accurately, and
- resolution of the data can be improved by using information from multiple probes at multiple frequencies.

Rotating probes usually consist of three coils spaced 120° apart (Fig. 2). Each coil scans the inner surface of the tube in a helical path. Since the probe speed is not constant, minor trigger pulses at 72° and major trigger pulses for each 360° rotation of the probe are generated and stored with the data. The

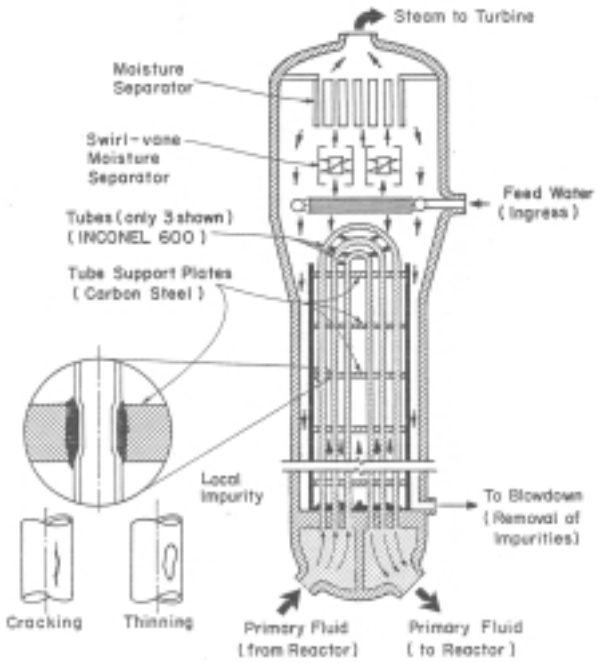

Fig. 1. Schematic diagram of a steam generator.

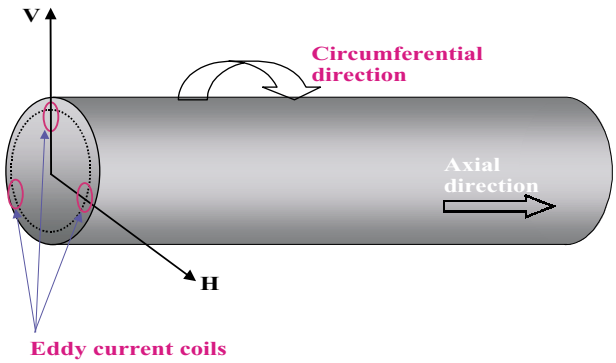

Fig. 2. Rotating probe geometry.

trigger signals can be used to display the data as a C-scan image with circumferential and axial directions along two axes. Three different probe types, namely pancake, axial and circumferential coil probes, are typically used. The axial and circumferential coils are sensitive to axial and circumferential flaws, respectively, whereas pancake coils are sensitive to both types of flaws. Each of these coils is excited at multiple frequencies.

An alternative configuration for the rotating probe uses two pancake and one plus-point coil probes. The plus point coil consists of two coils that are oriented orthogonal to each other [2]. Since the pickup coil configuration is differential, lift-off and magnetic effects due to geometry changes are significantly reduced, while axial and circumferential crack orientations are clearly distinguishable from each other. This is in contrast to conventional three-coil rotating probes, which are inefficient when interfering

Table 1
Rotating probe configurations and inspection frequencies

Probe types		Axial	Circumferential	Pancake (0.115″ diameter	HF Pancake (0.080″ diameter)	Plus-point
3RPC	Excitation	400, 300, 200	400, 300, 200	400, 300, 200, 20		
+RPC	frequencies (kHz)			300, 200, 100, 10	600, 300	300, 200, 100

signals from structures such as support plates are much stronger than those from cracks.

This paper deals with the automated analysis of rotating probe coil data, from two types of rotating probes. The first type will be referred to as the three-coil rotating probe coil (3RPC), while the second type of rotating probe will henceforth be referred to as the plus-point rotating probe coil (+RPC). The probe configurations, along with the excitation frequencies, are given in Table 1. The low-frequency channels (20 kHz or 10 kHz) are called locator channels and are used to locate and identify external support structures.

Automated eddy current signal processing techniques are extremely useful in the analysis of the large volume of data generated in a typical steam generator inspection. The primary objective of signal processing algorithms is to discriminate between defect signals and non-defect signals (such as those due to support structures or noise). In the case of defect signals, these algorithms can also determine defect parameters such as length, width and shape from the measurements. The first task is called signal classification or flaw detection while the second task is referred to as defect characterization.

One of the major problems in defect characterization is that of "smearing" due to the finite size of the probes used for inspection. An eddy current C-scan image is representative of the plan view of a defect and can be expressed by a convolution of the true surface dimension of the defect with a kernel that is derived from the probe footprint. The accurate characterization of a defect profile therefore requires application of a deconvolution algorithm [3] for removing the effect of probe geometry on the measured data. Deconvolution can also enhance the resolution of images from two closely spaced flaws.

Most deconvolution methods require prior knowledge of the kernel (point spread function or the probe response). This parameter, though vital for improving the performance of the algorithm, is often hard to obtain. A simple approach to deconvolution uses Wiener filters [4], where the form of the kernel is assumed. Blind deconvolution methods [3,5] are better suited to applications where the form of the kernel is unknown and must be estimated from the data at hand. This paper uses blind deconvolution based on the Richardson-Lucy algorithm [6,7] to estimate the true defect footprint. Advantages of this method include speed and the ability to incorporate constraints (for instance, constraints on the kernel) easily into the solution procedure.

The overall approach to data analysis is shown in Fig. 3. The raw eddy current data is first applied to a preprocessing stage. The goal of the preprocessing stage is to reduce the noise and enhance the signals obtained from eddy current probes. The enhanced data is applied to a feature extraction algorithm to identify features containing discriminatory information. Features selected are then applied to a classification algorithm, where defect signals are distinguished from non-defect signals, such as indications arising from benign external structures. Defect signals are then deconvolved to determine the true defect surface profile (defect characterization). Additional processing, such as signal compensation for various effects including lift-off, permeability and probe velocity, can also be performed before characterization, which estimates the 3D defect profile.

This paper is organized as follows. Section 2 describes the preprocessing steps used in the analysis of eddy current data obtained from the inspection of steam generator tubing. Section 3 describes the classification algorithms used while Section 4 outlines the deconvolution algorithm applied to recover

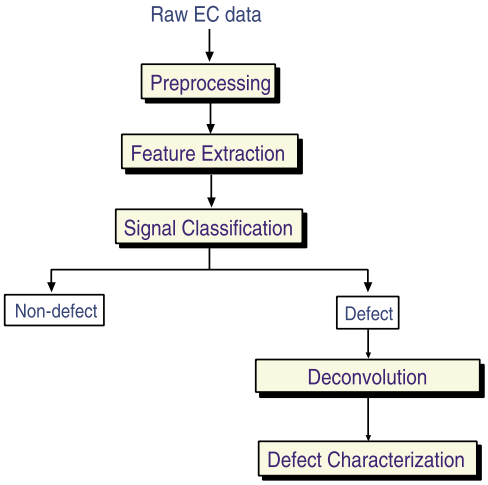

Fig. 3. Automated eddy current signal analysis.

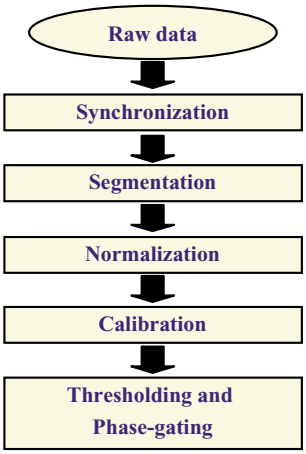

Fig. 4. Block diagram of the preprocessing algorithm.

the defect footprint. Typical results obtained at each step are also presented in their respective sections following the description of the procedures. Finally, Section 5 contains conclusions and suggestions for future work.

2. Signal preprocessing

A block diagram of the preprocessing algorithm is shown in Fig. 4. The raw data is one-dimensional in nature and a synchronization step converts the data into image format, which is easier to interpret. Both minor and major trigger pulses are used along with appropriate interpolation and decimation schemes to convert the one-dimensional stream into a 2D image where each column contains data from one rotation. Figure 5 illustrates the result of this process. Figure 5(a) shows the raw one-dimensional signal while Fig. 5(b) shows the result of synchronization. Synchronization is performed on both real and imaginary components of the data for all coils at all excitation frequencies.

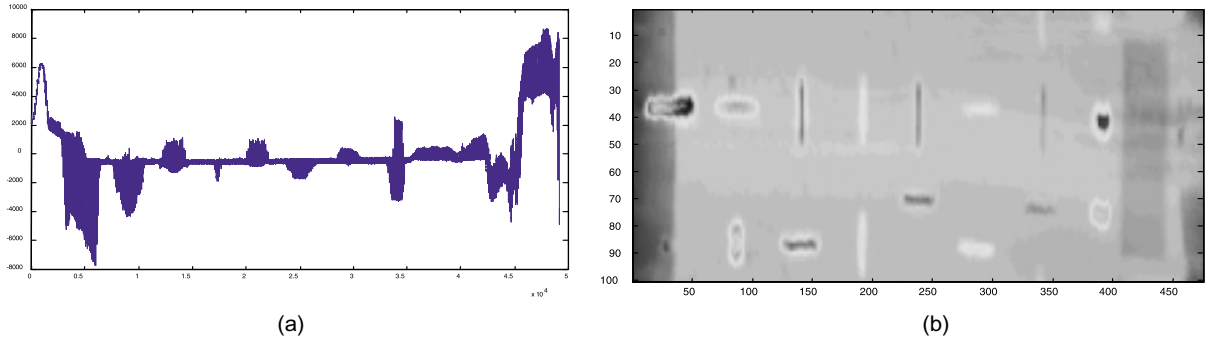

Fig. 5. Synchronization (a) raw data (b) synchronized image.

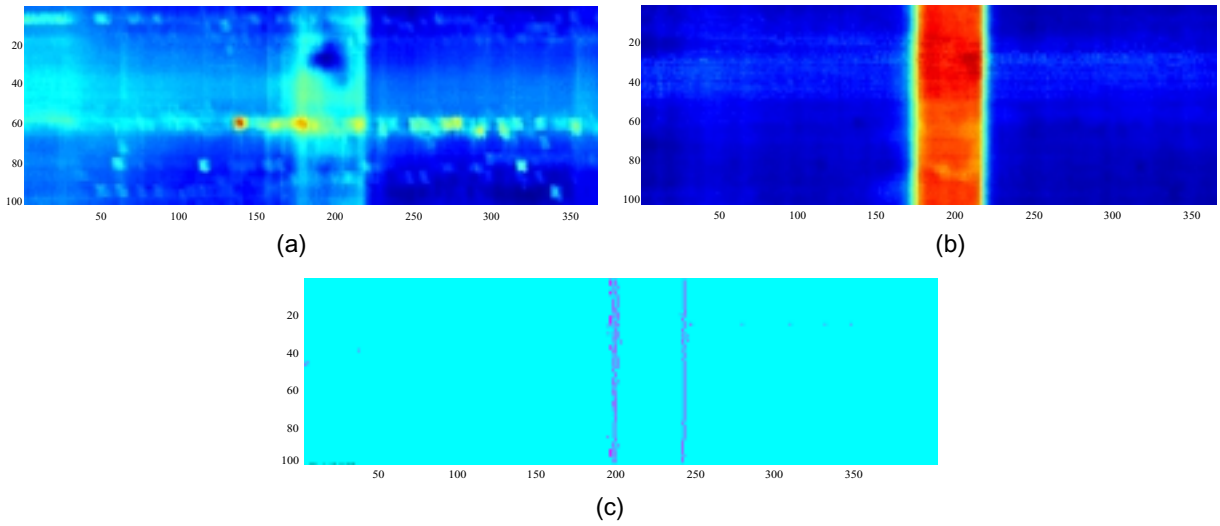

Fig. 6. (a) 400 KHz data, (b) 20 kHz data, (c) Sobel operator applied to 20 kHz data.

The next stage in the preprocessing procedure involves identification of support plates. Data segmentation is applied to detect tube support plate locations, which can be used as landmarks when flaws are identified. Data segmentation uses the locator channel data since data at lower frequencies are more sensitive to external support structures. Figure 6(a) shows typical data from a 400 kHz pancake coil, whereas Fig. 6(b) shows the corresponding 20 kHz data, obtained around a tube support plate region. Figure 6(c) shows the extracted edges of the tube support plates. The edges of the support plate can be clearly seen in Figs 6(b) and 6(c).

An edge enhancement operation using a Sobel edge detector [4] is used to identify the ends of the support plate. The source image can be represented by $f(x, y)$ where (x, y) denote the pixel locations of the image. The Sobel edge magnitude image $|\nabla f(x, y)|$ is given by

$$|\nabla f(x,y)| = \sqrt{\left(\frac{\partial f(x,y)}{\partial x}\right)^2 + \left(\frac{\partial f(x,y)}{\partial y}\right)^2} \tag{1}$$

The magnitude of $\nabla f(x, y)$ is then compared with a threshold T to determine candidate boundary

$S =$

-1		1
-2	(x,y)	2
-1		1

(a)

$t =$

-1	-2	-1
	(x,y)	
1	2	1

(b)

Fig. 7. Sobel operator filters. (a) vertical filter mask, (b) horizontal filter mask.

points. The threshold T is set at [8]

$$T = \sqrt{\beta(\mu^2 + \sigma^2)} \tag{2}$$

where β is a constant, μ is the mean, and σ is the variance of the image defined by

$$\mu = \frac{1}{MN} \sum_{x=1}^{M} \sum_{y=1}^{N} f(x, y) \tag{3}$$

$$\sigma = \frac{1}{MN} \sqrt{\sum_{x=1}^{M} \sum_{y=1}^{N} (f(x, y) - \mu)^2} \tag{4}$$

The Sobel edge detector can also be expressed as the convolution of $f(x, y)$ with the differential masks s and t, where s and t are the vertical edge detection filter and the horizontal edge detection masks respectively, and $*$ indicates the convolution operator. These masks are shown in Fig. 7.

Data normalization and calibration constitute the next two steps in the preprocessing procedure. Normalization consists of removing the mean value of the data from the synchronized image. Subtracting the d.c. bias also allows us to easily remove the contribution to the signal from the tube support plates.

Calibration is necessary to provide a reference for defect sizing. A reference (calibration) tube of the same material and dimensions as the tubes to be inspected is used for calibration. The calibration tube contains reference defects whose dimensions are known. Sample signals are then collected from both the calibration tube, as well as from actual tubes, using the same instrument settings. Signals from a reference defect are phase-rotated and scaled to a standard angle/amplitude. Typically, the phase angle of a reference through-wall hole is set to around 40° from the horizontal axis. This requires a rotation of the data by an angle θ given by

$$\theta = \theta_0 - \theta_R \tag{5}$$

where θ_0 is the phase angle of the through-wall hole and θ_R is the reference angle of the through-wall hole (40°). Inner-diameter (ID) flaws have phase angles of less than 40° while outer-diameter (OD) flaws make angles greater than 40°. Calibration of the raw data then involves rotating the raw data by the phase difference θ given above by multiplying each complex-valued data point by the rotation matrix

$$G_\theta = \begin{bmatrix} \cos\theta & \sin\theta \\ -\sin\theta & \cos\theta \end{bmatrix} \tag{6}$$

Figure 8 shows the vertical component of the eddy current data before and after calibration using phase rotation. Impedance plane plots are also shown to illustrate the effect of phase rotation.

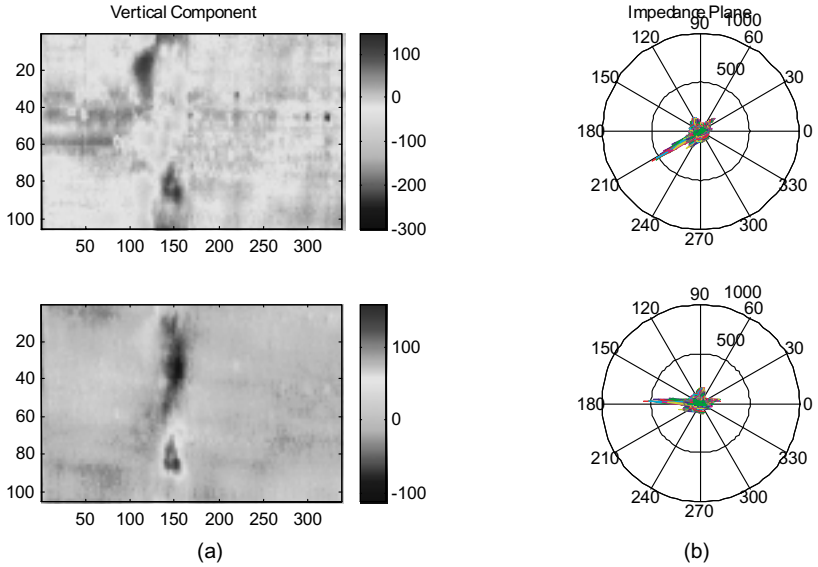

Fig. 8. Calibration by phase rotation (a) vertical component (b) impedance plane.

An additional step is necessary in the case of data from plus-point coils. The calibration procedure outlined above results in the data from plus-point coils being sensitive to only axial flaws. Data from circumferential flaws is 180° out of phase with data from axial flaws. The plus-point data is therefore rotated by 180° to create an additional set of channels that are sensitive to circumferential flaws.

The calibration procedure results in signals from all defects lying between 0° and 180° in the impedance plane in the absence of measurement noise. A phase gating step is applied to retain only those signals that lie between the two limits. In practice, phase gating retains all signals that satisfy

$$\varepsilon \leqslant \theta_s \leqslant 180 - \varepsilon \tag{7}$$

where θ_s is the phase angle of the signal, and ε is a small phase angle used to limit the effect of noise. The effect of phase gating can be clearly seen in Fig. 9.

3. Signal classification

3.1. Feature extraction and classification

The phase-gated data, in most cases, only retain signals from defects. However, there is some residual noise present and the data must therefore be classified to identify the presence of defects. A first step in this direction is the extraction of features that can discriminate between defects and non-defects. Additional classification steps can also be applied to discriminate between different kinds of defects. Various features considered for classification include the area of the region of interest (ROI), the maximum, minimum and mean phase angles in the indication, the phase spread and the volume V of the ROI. The features are computed for both the real and imaginary components of the signals from all coils at all frequencies. In the nuclear industry, the real and imaginary components are referred to as the horizontal and vertical components respectively. We use these terms interchangeably throughout the rest of this paper.

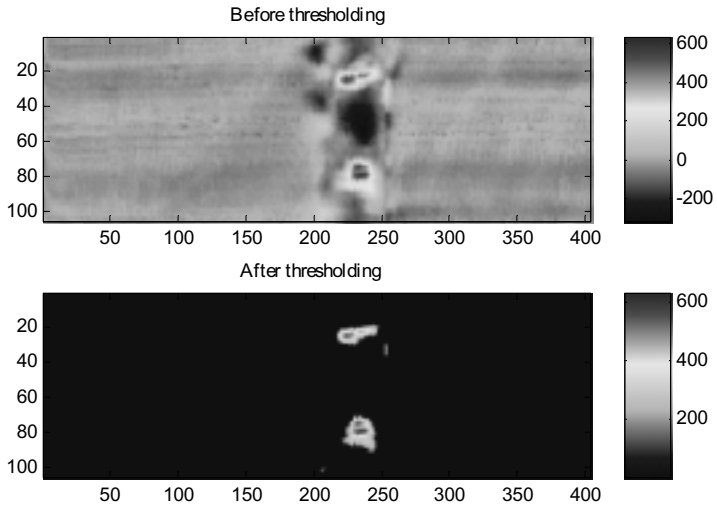

Fig. 9. Thresholding by phase gating (a) before (b) after phase gating.

A decision tree based algorithm is then used to identify key features that have the maximum amount of discriminatory information. The algorithm uses concepts from information theory to select the feature that maximizes the classification performance at each stage of the decision tree. By performing this operation iteratively at each level of the decision tree, the algorithm obtains the best possible subset of features for optimal classification. This subset of features is saved and used for classification.

The decision tree algorithm was applied to identify the optimal feature subset for the following classification tasks:

– 3RPC Data

  ∗ Defect vs. Non-defect
  ∗ Multiple Axial Indications (MAI) vs. Single Axial Indications (SAI)

– +RPC Data

  ∗ Defect vs. Non-defect
  ∗ Axial flaws vs. Circumferential flaws
  ∗ Multiple Axial Indications (MAI) vs. Single Axial Indications (SAI)

The feature subset identified by the decision tree for each task was different. The selected feature subsets were then applied to the classification algorithm.

A hierarchical signal classification scheme is used for classification of RPC eddy current data (Fig. 10). The first stage of the hierarchical system classifies data as either a defect or a non-defect. Defects are further classified into one of several classes using additional hierarchical classifiers. In this study, we use multilayer perceptron (MLP) neural networks [9] as the classifiers at each stage. This system has several advantages over conventional classification algorithms using a single classifier to distinguish between several classes. The primary advantage of the hierarchical classification system is its modularity. Data from additional classes can be handled easily by adding more classification modules without the need for retraining existing classifiers. Furthermore, breaking up the classification task into several simpler tasks also simplifies the neural network design and reduces training times. There is also some evidence to suggest that such a system performs better when compared to a single neural network [9].

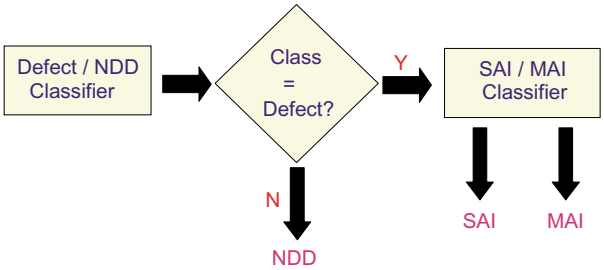

Fig. 10. Hierarchical signal classification.

Table 2
Training and test data distribution for 3RPC probes

	Training database	Test database
Total defects	12	8
MAI	6	4
SAI	6	4
Non-Defects	12	8

Table 3
Data distribution for +RPC data

	Comments	Training database	Test database
Total defects		20	18
MAI	Axial	10	9
SAI		4	3
Circumferential		6	6
Non-defects		19	19

3.2. Results

The feature extraction and classification algorithms were applied to data collected using both 3RPC and +RPC probes. A total of forty data files collected with the 3RPC probe were used to evaluate the hierarchical signal classification technique. These forty files were equally distributed between defects and non-defects. Of the twenty defect files, there were 10 files each from MAI and SAI indications. The training data distribution for the 3RPC probe is shown in Table 2. Similarly, Table 3 shows the data distribution for +RPC data.

Initial results of classification for 3RPC data are shown in Tables 4 and 5. Table 4 shows the first stage classification result (defect vs. non-defect) while Table 5 shows the second stage classification result (MAI vs. SAI). A single hidden layer MLP with six hidden layer neurons was used for defect/non-defect classification. The input and output layers had three neurons (the number of features) and two neurons (number of output classes), respectively. Similarly, a single hidden layer MLP with five hidden layer neurons was used for MAI/SAI classification. These results indicate that the hierarchical classification algorithm, in conjunction with the features selected by the decision tree, can classify the data with a high level of accuracy. Similar results for +RPC data are shown in Table 6 (defect vs. non-defect, single hidden layer MLP with six neurons), Table 7 (Axial vs. Circumferential, single hidden layer MLP with four neurons) and Table 8 (MAI vs. SAI, single hidden layer MLP with four neurons). The classification algorithm obtained 100% correct classification on all classification tasks with +RPC data. However, these results must be viewed with some caution, since the training and test databases were extremely limited. Evaluation of the algorithm on additional data is currently being performed.

Table 4
Classification performance (3RPC data, stage 1)

True class	Classification	Defect	Non-defect
Defect		7	1
Non-defect		1	7

Table 5
Classification performance (3RPC data, stage 2)

True class	Classification	MAI	SAI
MAI		3	1
SAI		0	4

Table 6
Classification performance (+RPC data, stage 1)

True class	Classification	Defect	Non-defect
Defect		18	19
Non-defect		0	0

4. Blind deconvolution of eddy current data

Characterization of defects is an important part of the analysis procedure. The major requirement in characterization is identifying the defect shape and parameters, such as length, width and depth. In this study, we concentrate on identifying the length and width of the defect (also called the defect footprint). As mentioned earlier, precise identification of the footprint is difficult due to the blurring effect of the probe. We model the inspection procedure as a convolution between the true defect footprint and the probe kernel. Doing so enables us to use deconvolution methods for recovering the true footprint. Blind deconvolution methods are particularly attractive since they do not require specification of a kernel. These algorithms iteratively estimate the kernel from the available data. Another advantage of a blind deconvolution algorithm is the ease with which constraints can be added. We take advantage of this property to constrain the size of the kernel based on the size of the probe used.

The blind deconvolution algorithm used in this study is the Richardson-Lucy algorithm [6,7]. This algorithm is based on Bayes's theorem and was initially derived by Richardson and Lucy in the early 1970's. The algorithm uses the maximum likelihood principle and is able to obtain high quality reconstructed images even in the presence of noise. The algorithm has been extensively applied in astronomy and medical imaging in the past [10].

4.1. The Richardson-Lucy algorithm

We start with a brief review of the Richardson-Lucy algorithm. The Richardson-Lucy algorithm is based on Bayes's theorem

$$P(x|y) = \frac{P(y|x)P(x)}{\int P(y|x)P(x)dx} \tag{8}$$

where $P(y|x)$ is the conditional probability of an event y, given the event x and $P(x)$ is the probability of event x. In deconvolution, $P(x)$ and $P(y)$ are identified as the original image distribution $f(x)$ and the convolved (or measured) image $c(x)$ respectively [5,6]. Also, the conditional probability $P(y|x)$ is

Table 7
Classification performance (+RPC data, stage 2)

True class	Classification	Axial	Circumferential
Axial		12	0
Circumferential		0	6

Table 8
Classification performance (+RPC data, stage 3)

True class	Classification	MAI	SAI
MAI		9	0
SAI		0	3

identified as the kernel function or the PSF centered at x, i.e., $g(y,x)$. This can be used to derive the iterative form of the deconvolution algorithm:

$$f_{i+1} = \int \frac{g(y,x)c(y)dy}{\int g(y,x)f_i(z)dz} f_i(x) \tag{9}$$

where i is the iteration number. For image restoration, Eq. (9) can alternatively be written as

$$f_{i+1}(m,n) = \left\{ \left[\frac{c(m,n)}{f_i(m,n) * g(m,n)} \right] * g(-m,-n) \right\} f_i(m,n) \tag{10}$$

where $*$ denotes the convolution operation. All quantities in Eq. (10) are two-dimensional in nature and depend on two spatial variables m and n. Given the PSF $g(m,n)$ and an initial guess of the original image $f(m,n)$, the reconstructed image can be obtained by iteratively applying Eq. (10) until convergence is achieved.

Blind deconvolution algorithms however do not have access to the kernel and must estimate the kernel from the data. The kernel can be estimated by using the expression given in Eq. (11), called the inverse iterative equation [5]. The inverse iterative equation is derived by reversing the role of the reconstructed image and the PSF in Eq. (10) and is given by

$$g_{i+1}(m,n) = \left\{ \left[\frac{c(m,n)}{g_i(m,n) * f^{k-1}(m,n)} \right] * f(-m,-n) \right\} g_i(m,n) \tag{11}$$

The inverse iterative equation is also referred to as a Richardson-Lucy operation.

The blind deconvolution algorithm consists of a two-step procedure. At the kth iteration, the PSF $g^k(y,x)$ is calculated from Eq. (12) by performing a specific number of Richardson-Lucy operations, given the knowledge of the reconstructed image $f^{k-1}(m,n)$ obtained after the $k-1$th iteration:

$$g^k_{i+1}(m,n) = \left\{ \left[\frac{c(m,n)}{g^k_i(m,n) * f^{k-1}(m,n)} \right] * f^{k-1}(-m,-n) \right\} g^k_i(m,n) \tag{12}$$

Here, k denotes the iteration number and i denotes the number of Richardson-Lucy operations during each iteration. The new estimate of the deconvolved image $f^k(m,n)$ is obtained by performing the same number of Richardson-Lucy operations (Eq. (13)), given the PSF $g^k(y,x)$ obtained from Eq. (12) above.

$$f^k_{i+1}(m,n) = \left\{ \left[\frac{c(m,n)}{f^k_i(m,n) * g^k(m,n)} \right] * g^k(-m,-n) \right\} f^k_i(m,n) \tag{13}$$

These two steps are repeated until convergence is achieved.

Fig. 11. Results of preprocessing (a) Defect signal (b) Signal after thresholding (c) Signal after preprocessing.

4.2. Blind deconvolution of eddy current signals

Application of blind deconvolution to eddy current data is not straightforward due to various factors that affect the signal. These factors include variation of probe scanning speed, liftoff and measurement noise. In order to use the blind deconvolution procedure, we assume the probe response to be locally invariant and select a small section of data (the ROI) around the defect signal as input to the deconvolution algorithm. A preprocessing step is necessary to denoise the data and automatically select the ROI. This preprocessing algorithm performs the following operations:

1. Threshold the eddy current data image $d(m,n)$, using
$$\overline{d}(m,n) = \begin{cases} 0 & d(m,n) \leqslant T \\ d(m,n) & d(m,n) > T \end{cases} \tag{14}$$
where the threshold value T is given by $T = \alpha\sigma$, σ is the standard deviation of the data and α is a constant.
2. Calculate a binary image $M(m,n)$ from $\overline{d}(m,n)$:
$$M(m,n) = \begin{cases} 0 & \overline{d}(m,n) = 0 \\ 1 & \overline{d}(m,n) > 0 \end{cases} \tag{15}$$
3. Use binary morphological closing and opening operations [4] to eliminate any isolated pixels from $M(m,n)$. The structuring element used in the morphological operations is a 3×3 mask. This operation results in a new binary image $M'(m,n)$.
4. The denoised data $D(m,n)$ is then obtained by a pixel-by-pixel product of $d(m,n)$ and $M'(m,n)$:
$$D(m,n) = \overline{d}(m,n) \cdot M'(m,n) \tag{16}$$

Figure 11 shows an example of the results of preprocessing for a single data file. The results clearly show the improvement in data quality after preprocessing. The ROI can now be easily selected from the preprocessed data and applied to the blind deconvolution algorithm described above. The deconvolution algorithm is summarized below.

1. Initialize kernel estimate $g(m,n)$ and defect footprint $f(m,n)$.

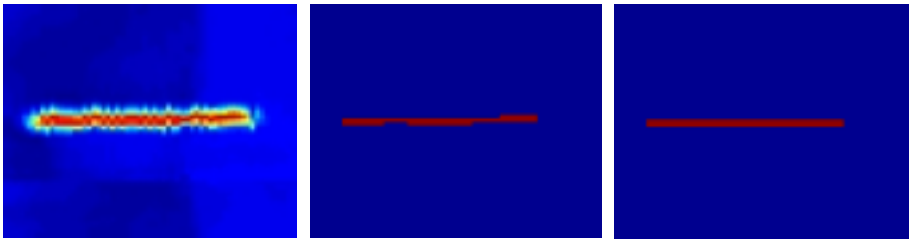

Fig. 12. Blind deconvolution of eddy current measurements from an axial rectangular defect (a) Defect signal (b) Deconvolution result and (c) true defect footprint.

2. Estimate the new kernel iteratively using the measurement $c(m,n)$ using

$$g_{i+1}^{k}(m,n) = \left\{ \left[\frac{c(m,n)}{g_i^k(m,n) * f^{k-1}(m,n)} \right] * f^{k-1}(-m,-n) \right\} g_i^k(m,n) \tag{17}$$

3. Estimate the defect footprint iteratively using

$$f_{i+1}^{k}(m,n) = \left\{ \left[\frac{c(m,n)}{f_i^k(m,n) * g^{k}(m,n)} \right] * g^{k}(-m,-n) \right\} f_i^k(m,n) \tag{18}$$

4. Repeat steps 2 and 3 until convergence is achieved. The convergence condition is given by

$$C\left(f^k(m,n), f^{k-1}(m,n)\right) = \frac{\sum_{m,n} \left(f^k(m,n) - f^{k-1}(m,n)\right)^2}{\sum_{m,n} f^k(m,n)^2} \tag{19}$$

4.3. Results

Data obtained from eddy current inspection of both calibration tubes and field tubes was used to evaluate the performance of the blind deconvolution algorithm. Figure 12 shows results of applying blind deconvolution to data obtained from eddy current inspection of calibration tubes. The flaw is rectangular in shape, 0.5″ long and 0.02″ wide. Figure 12(a) shows the magnitude of the impedance measurement obtained from a 0.080″ diameter rotating pancake coil at 400 kHz. Figure 12(b) shows the resultant footprint obtained after deconvolution while Figure 12(c) shows the true defect footprint. The length of the defect as estimated from the raw data is 0.57″ while the length of the defect as estimated from the deconvolution result is 0.5″.

Deconvolution is especially useful in cases where there are multiple flaws in close proximity but the measurement appears to be from a single flaw because of the blurring effect of the probe. An example of this is shown in Fig. 13. Deconvolution in this case results in the separation of two close axial flaws. This helps in characterizing the sample as a multiple axial indication (MAI).

These results indicate that the blind deconvolution algorithm is a powerful tool for properly characterizing defects in steam generator tubes. The results presented show that the deconvolution algorithm improves estimates of the defect length and width and is capable of separating two or more flaws in close proximity. This capability is very important for the nuclear industry, since, in many cases, it is very difficult to accurately estimate the severity of degradation from the raw eddy current measurement.

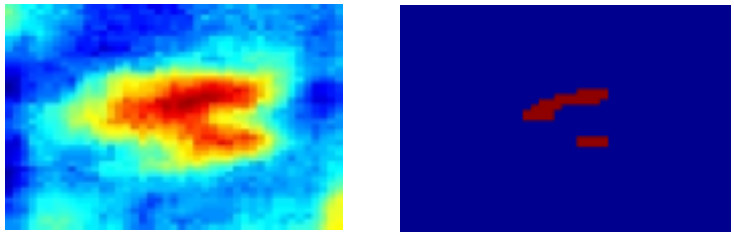

Fig. 13. Blind deconvolution of eddy current measurements from MAI defect (a) Defect signal and (b) Deconvolution result.

5. Conclusions

An automated signal analysis algorithm for eddy current data from steam generator tubes was described. The algorithm converts the data into a visually appealing format and analyses it to determine the presence or absence of flaws. The analysis algorithm can also indicate the type of degradation accurately. A blind deconvolution algorithm is also proposed for accurately characterizing defects and determining the defect footprint. Preliminary results indicate that the algorithm can classify and characterize data from both 3RPC and +RPC probes. However, the algorithms need to be evaluated on a more diverse database. This task is currently underway.

References

[1] L. Udpa and W. Lord, New approaches for multifrequency ECT of steam generator tubes, *Proc. of the ISMM Int. Symposium*, ACTA Press, Honolulu, USA, (February 1988), pp. 108–112.
[2] J. Siegel, Detecting SG tube cracks in difficult places, *Inspection* (January 1996), 18–19.
[3] M.R. Banham and A.K. Katsaggelos, Digital image restoration, *IEEE Signal Proc. Magazine* **14**(2) (March 1997), 24–41.
[4] R.C. Gonzalez and R.E. Woods, *Digital Image Processing*, Addison-Wesley, Reading, MA, 1992.
[5] D.A. Fish, A.M. Brinicombe, E.R. Pike and J.G. Walker, Blind deconvolution by means of the Richardson-Lucy algorithm, *J. Opt. Soc. Am. A* **12**(1) (January 1995), 58–65.
[6] W.H. Richardson, Bayesian-based iterative method of image restoration, *J. Opt. Soc. Am. A* **62**(1) (January 1972), 55–59.
[7] L.B. Lucy, An iterative technique for the rectification of observed distributions, *Astronomical Journal* **79**(6) (June 1974), 745–754.
[8] G.X. Ritter and J.N. Wilson, *Handbook of computer vision algorithms in image algebra*, CRC Press, New York, 1996.
[9] S. Haykin, *Neural networks: A comprehensive foundation*, Macmillan International, New York, 1994.
[10] L.A. Shepp and Y. Vardi, Maximum likelihood reconstructions for emission tomography, *IEEE Trans. Med. Imaging* **MI-1** (1982), 113–122.